*J Mater Sci: Mater Electron* (2021) 32:611–622

# Properties of a facile growth of spray pyrolysis-based rGO films and device performance for Au/rGO/n-InP Schottky diodes

Fulya Esra CİMİLLİ ÇATIR[1,*]

[1] *Department of Electronic Technologies, Vocational School, Erzincan Binali Yildirim University, 24200 Erzincan, Turkey*

**Received:** 6 July 2020
**Accepted:** 5 November 2020
**Published online:** 13 November 2020

© Springer Science+Business Media, LLC, part of Springer Nature 2020

## ABSTRACT

In this study, the reduced graphene oxide (rGO) was synthesized from graphene oxide (GO) by using chemical reduction method. The spray pyrolysis technique was used to deposit rGO film on n-InP substrate. The structural, morphological, and optical properties of rGO film were investigated by XRD, SEM, and UV–Vis spectroscopies. Au/rGO/n-InP device was fabricated and the current–voltage characteristics were examined in the temperature range of 60–300 K. The device parameters of barrier height (BH) and ideality factor are found to be strong functions of temperature due to the barrier inhomogeneities at metal–semiconductor interface. The temperature dependency of the electrical characteristics of the Au/rGO/n-InP SBD was explained by the thermionic field emission (TFE) theory with Gaussian distribution (GD) of the BH values. The BH has a GD with a mean barrier height of $\overline{\Phi}_{bo}$ = 0.93 eV between 120 and 300 K temperatures and $\overline{\Phi}_{bo}$ = 0.62 eV between 60 and 120 K temperatures. It was seen that the existing current mechanism is predominantly controlled by space-charge-limited current (SCLC) at large forward bias according to the sample temperature. The rGO interface plays also an important role in the conduction mechanism and electronic properties of the device.

## 1 Introduction

Graphene, as a 2D material, is the most attractive member of carbon-based materials due to its significant electrical, optical, and mechanical properties [1]. Moreover, graphene is the strongest, stiffest and thinnest material ever known with ultra-large specific surface area. As a result, graphene-based composites, 2D film materials, and coated substrates are extensively explored in electronic circuit industry. On the other hand, the zero-band gap of graphene limits its use in nano-electronics, such as field-effect transistors [2]. Recently, the graphene oxide (GO) and reduced graphene oxide (rGO) have become the standard graphene precursors because a gradual reduction of oxygen concentration of graphene oxide is known as an alternative way to tune the band gap of graphene.

Address correspondence to E-mail: fcatir@erzincan.edu.tr

https://doi.org/10.1007/s10854-020-04843-0

Many graphene synthesis methods have been developed academically and industrially and still in progress. The most usual methods are obtaining graphene by chemical reduction, such as sodium boron hydride or hydrazine or by thermal reduction of graphene oxide by exposure to high temperatures which is called reduced graphene oxide (rGO) [1]. While the graphene oxide is reduced to reduced graphene oxide by thermal method, the sample needs to be annealed at approximately 2000 °C. However, such annealing at high temperatures is not suitable for all substrates types [3]. On the other hand, low-temperature annealing (< 500 °C) cannot remove the oxygen functional groups at all, that is, thermal annealing may not be a suitable method when considered alone. Poorali et al. compared chemical and physical reduction methods to prepare layered graphene with graphene oxide and found that the modified graphene by hydrazine hydrate treatment had the best structural properties among others [4].

Metal–semiconductor (MS) devices are very important for electronic device applications and they are mostly used as rectifiers, inverters, photodiode, field-effect transistors (FETs), solar cells, and photodetectors [5]. Among III-V semiconductors, indium phosphide (InP) has attracted much interest due to increasing demand in the microelectronics industry for suitable optoelectronic and fast-switching devices [6]. In addition, InP preferred as an alternative to Si in MS contacts because of its high electron mobility and direct band gap [7]. So, InP-based materials have a wide range of uses in optoelectronic (solar cells and detectors) and microwave (field-effect transistors) devices. However, serious drawbacks of InP substrates in MS devices (especially n-type) are the low Schottky barrier height of metal contacts and the difficulty in surface quality control, which result in increased Schottky leakage currents and a degradation of the device performance.

In MS Schottky devices, the electrical and electronical properties of these devices can be changed by adding an interlayer between the metal and the semiconductor [8, 9] and their performance highly influenced by the interface film quality [10]. It is reported that the junctions formed from reduced graphene oxide have a rectifying feature [11]. For example, the rGO-Rh101 nanocomposite/p-Si heterojunction was fabricated and it exhibited good rectifying behavior [12]. The ideality factor and barrier height values of this device were calculated from the current–voltage measurements and the barrier height was confirmed to be inhomogeneous. In another study, Azmi et al. produced back-to-back rGO/Si Schottky device. Series resistance, barrier height, and ideality factor were investigated from the current–voltage (*I-V*) measurements at different temperatures and they found that the barrier height of rGO/Si Schottky structure was inhomogeneous at the interface [13]. A Gaussian distribution was observed with mean barrier height of 1.23 and 0.16 eV, respectively. Pandit et al. reported the characteristics of reduced graphene oxide rGO/GaN Schottky structure performed at various temperatures and they indicated that reduced graphene oxide interlayer was a promising material as a transparent conductive electrode for high-performance UV photodiodes [14].

The most important property of the graphene-based Schottky contact is that barrier height can be adjusted by changing the graphene working function by chemical doping. This advantage not only makes it easy to design and change the electrical characteristics of the diode but also allows them to be used as chemical sensors and photodetectors [13]. However, despite these important properties of graphene, little is known about graphene-based Schottky barrier diode (SBD), their electrical properties, and device performance. On the other hand, a verified theory has not yet been developed for organic film-based Schottky diodes with an inhomogeneous Schottky contact [15]. Also, the analysis of the forward bias current–voltage (*I-V*) characteristics of SBD parameters only at room temperature does not provide detailed information about their current conduction mechanism and barrier formation at metal–semiconductor interface [16]. In addition, only the temperature-dependent *I-V* measurements in a wide temperature range gives enough information to determine the current conduction mechanisms of SBDs. In addition, the *I-V* characteristics of the MS contacts usually deviate from the ideal thermionic emission (TE) current model [7, 17–19], which reveals a decrease in the barrier height (BH), while an increase in the ideality factor with decreasing temperature qq. Especially, the decrease in the BH at low temperatures leads to nonlinearity in the activation energy plot and this behavior can be attributed to the presence of Schottky barrier height (SBH) inhomogeneity [17, 20, 21]. On the other hand, the current across the MS contact is greatly influenced by the

presence of the SBH inhomogeneity [20, 21]. In such case, the charge carriers flow through the lower barriers/patches at low temperatures; therefore, TE theory reveals high n values. Thus, several other conduction mechanisms, such as thermionic field emission (TFE), field emission (FE), generation-recombination, tunneling, space-charge-limited current (SCLC), and trap-charge-limited current (TLCL) [22–24], and also the Gaussian distribution of the barrier height contributes to the MS current [19, 25].

In addition, there are few studies [13, 26] of a detailed analysis about the temperature-dependent *I-V* characteristics of graphene-based InP Schottky devices. This is important for better understanding of reduced graphene oxide role in the interface of the metal–semiconductor Schottky devices. Herein, the aim of this study is to examine the reduced graphene oxide film structure in detail and to investigate the temperature-dependent *I-V* characteristics of the Au/rGO/n-InP Schottky device in a wide temperature range for technological applications. Current transmission mechanisms of Au/rGO/n-InP Schottky were investigated and explained.

## 2 Experimental

In this study, reduced graphene oxide was produced from graphene oxide by a chemical reduction method. For reduction of the graphene oxide, firstly, 1 g of graphene oxide powder was dispersed in 100 ml of deionized water and mixed for 24 h at 30 °C in a beaker with a magnetic stirrer, then treated for 3 h in an ultrasonic bath. After ultra-sonication, 30 mL of hydrazine hydrate ($N_2H_4.H_2O$) was added, and the mixture was placed in an oil bath, stirred, and maintained at 90 °C on a hot plate magnetic stirrer for 24 h. The mixture was left to cool at room temperature. After this duration, the mixture was first washed with acetone, then washed with deionized water, and finally filtered. The color of the mixture indicates that reduced graphene oxide was obtained when the color changed from dark brown to black (Fig. 1). After this process was repeated twice, the material remaining in the filter was dried in the oven at 80 °C for 24 h and reduced graphene oxide was obtained in powder form.

Produced reduced graphene oxide was dispersed in deionized water, dimethylformamide (DMF), and DMF/DI (1/1%) solvents. Au/rGO/n-InP Schottky barrier diode (SBD) was fabricated by using n-InP (100) wafer. To remove the impurities and surfaces damages, n-InP semiconductor was degreased in trichloroethylene, acetone, and methanol for 5 min each step by using ultrasonic agitation, and etched with hydrofluoric acid (48%) and $H_2O$ solution (1:10) within 1 min. It was washed quickly with deionized water and dried well with nitrogen ($N_2$) gas. 99.9% purity of indium metal (In) was formed with thickness of 150 nm at a pressure about $10^{-6}$ mbar in NANOVAK NVTH-350 high vacuum system and ohmic contact was performed by annealing at 350 °C for 1 min under $N_2$ atmosphere. The InP substrate with ohmic contact was divided into two parts: One part was used to produce the reference Au/n-InP/In diode, and the other part was covered with reduced graphene oxide film to produce the Au/rGO/n-InP diode.

The reduced graphene oxide film was deposited by spray pyrolysis technique with Holmarc's HD-TH-04 Spray Pyrolysis system. The rGO film was deposited on the substrates with a thickness of 100 nm. The deposition temperature was 200 °C and compressed and filtered air was used as carrier gas. The distance between the nozzle and the substrate was 30 cm. The reduced graphene oxide film was simultaneously grown onto both glass and InP semiconductor substrates and dried at 100 °C for 15 min under $N_2$ gas flow. According to spectroscopic and morphological analyses, it was determined that reduced graphene oxide was successfully coated on semiconductor surface. Schottky junction was formed by using Au (99.9%) metal deposited on the rGO film as circular dots with 150 nm thickness (0.5 mm diameter) under $10^{-6}$ mbar by vacuum evaporation system. Schematic diagram of Au/rGO/n-InP device is given in Fig. 2. The XRD pattern was collected on a XRD diffractometer using Cu Kα ($\lambda$ = 1.5406) as the X-ray source at a scanning rate of 1 ° $min^{-1}$ and generator voltage and current was 40 kV and 30 mA, respectively. The surface morphology of the reduced graphene oxide film was carried out by Zeiss Supra 50 VP Scanning electron microscopy (SEM). The optical absorption and transmittance of reduced graphene oxide film on glass substrate were performed using Perkin-Elmer Lambda 2S UV–VIS. spectrophotometer. The *I–V* measurements of the Au/rGO/n-InP Schottky barrier diode (SBD) was obtained by using a Keithley 2400 and a 6514 Keithley electrometer. The temperature dependent *I–V* measurements were performed

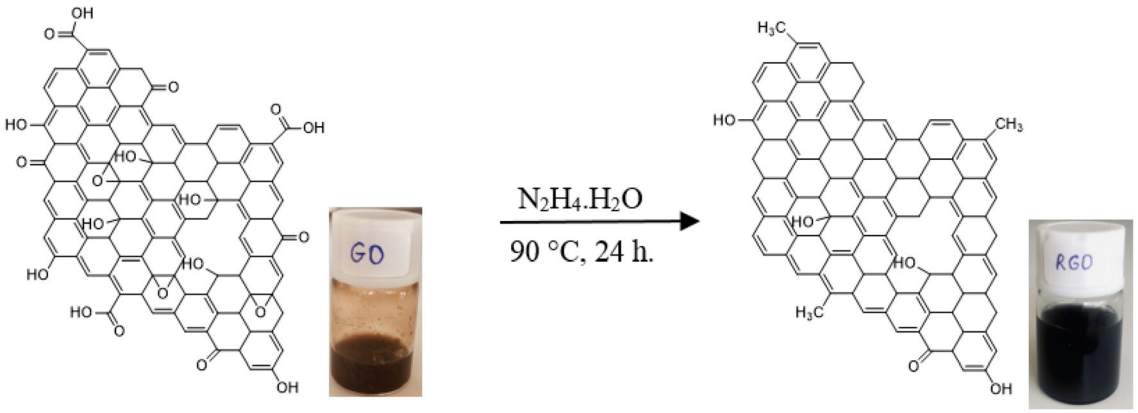



**Fig. 1** Chemical reduction of graphene oxide to reduced graphene oxide

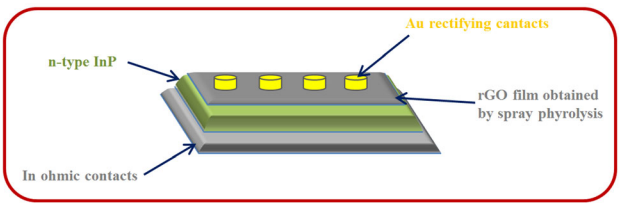



**Fig. 2** Schematic diagram of Au/rGO/n-InP device

by using He cryostat with 10 K temperature steps at 60–300 K temperature range under dark conditions.

## 3 Results

The structural and optical characteristics of the reduced graphene oxide film were analyzed by using X-ray diffraction (XRD), scanning electron microscopy (SEM), and absorbance–transmittance measurements. The XRD spectra show that the rGO film has a strong diffraction peak at 26.5369 for the (002) lattice plane as shown in Fig. 3. It shows highly crystalline nature of reduced graphene oxide and the interplanar spacing (d) value calculated from Bragg's

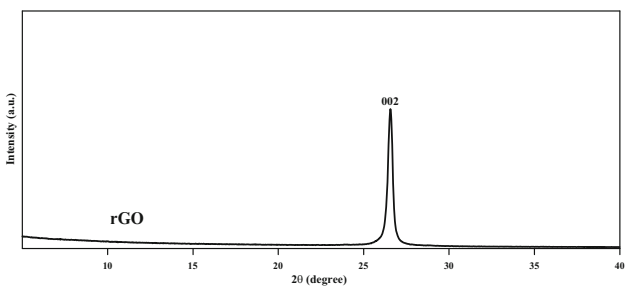



**Fig. 3** XRD spectra of reduced graphene oxide obtained by spray pyrolysis technique

law ($n\,\lambda = 2d\sin\theta$) as 3.35623 Å. Similar results were found for XRD diffractograms of rGO films in the literature [12, 27, 28].

Figure 4 shows the morphology and structure of the reduced graphene oxide nanosheets investigated using scanning electron microscopy (SEM). It is clearly seen that paper-like structures with ripples and wrinkles on the surface. These properties in the graphene lattice can be created by rebuilding C sp2 bonds as a result of reducing the graphene oxide to reduced graphene oxide. EDX measurements show that the C/O ratio increased from 1.18 to 3.74 by weight percent after the chemical treatment. Thus, we can conclude that the weight percent of C/O increases with the chemical treatment of the rGO film and it contributed significantly to the reduction of graphene oxide to reduced graphene oxide. As a result, the graphene oxide has been successfully reduced to reduced graphene oxide. Also, as seen from reduced graphene oxide film morphologies, the spray pyrolysis technique is a convenient technique to deposit thin films on a semiconductor.

UV–visible spectroscopy was used for the optical characterization of reduced graphene oxide. Figure 5a shows an absorption peak at about 270 nm for rGO similar to $\pi \rightarrow \pi^*$ transitions of aromatic C–C bands that is attributed to decrease in oxygen containing functional groups to carbon–carbon double bonds (C = C), which confirms the successful reduction of graphene oxide to reduced graphene oxide. Graphene is known as almost transparent with more than 98% optical transmittance [29]. Figure 5b demonstrates that the transmittance increases throughout the visible region and shows a transmittance of 85.1% at 665 nm wavelength. In addition, as

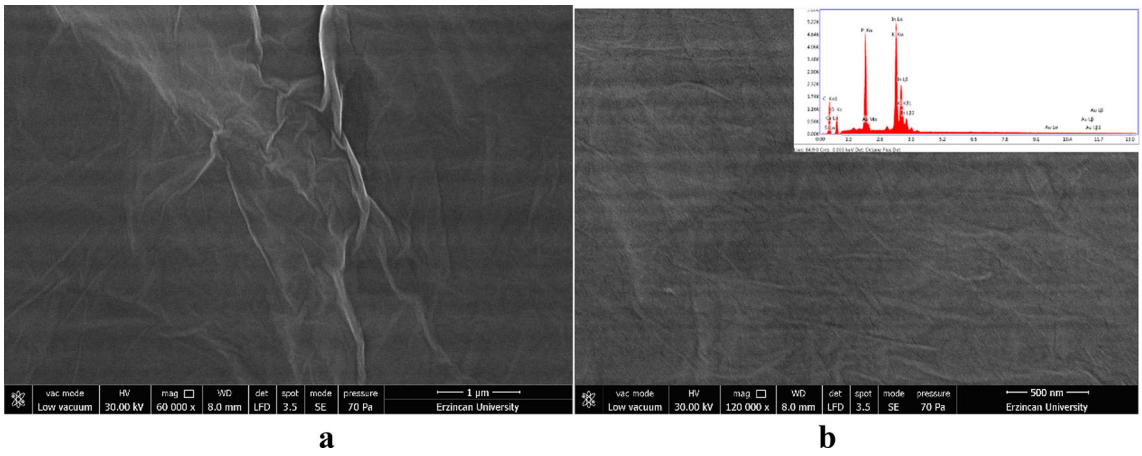



**Fig. 4** **a** SEM micrograph of rGO film, **b** SEM micrograph and EDX measurement of rGO film

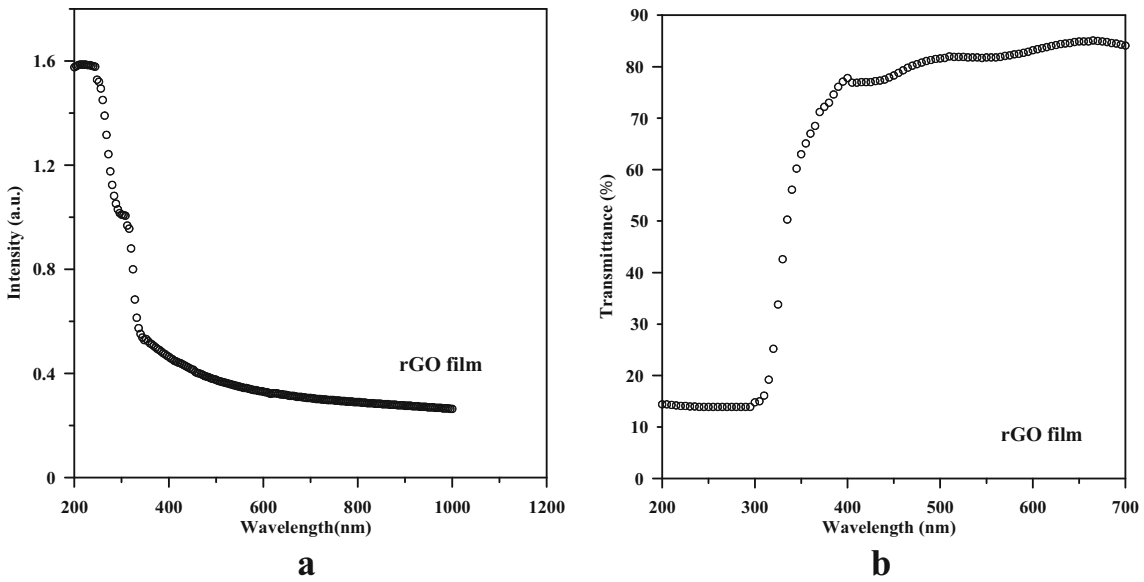



**Fig. 5** **a** Absorbance, **b** transmittance spectrum of reduced graphene oxide film

shown in Fig. 5, absorbance and transmittance spectrums of rGO are consistent with each other. Moreover, these ultra-thin layers have been shown to be transparent.

Figure 6a indicates a comparison of the *I-V* characteristics of Au/n-InP reference diode and Au/rGO/n-InP at 300 K. *I–V* characteristics of the diode for sample temperature from 60 to 300 K with 10 K steps are given in Fig. 6b. The Au/rGO/n-InP device has good rectifying properties at room temperature and between the temperature range 60 and 300 K. It is clear that temperature rise or fall does not change the rectification properties of the device. This result demonstrates that Au/rGO/n-InP device is suitable to use at wide temperature ranges [30].

Barrier height (BH) and ideality factor ($n$) calculation of the Schottky diodes were calculated by using thermionic emission (TE) theory. Schottky contact current ($I$) is described according to TE theory given by the following relation [22]:

$$I = I_0 \exp\left(\frac{q(V - IR_s)}{nkT}\right)\left[1 - \exp\left(-\frac{q(V - IR_s)}{kT}\right)\right], \quad (1)$$

where $I_0$ is the saturation current and can be calculated from intercept value of the linear portion of *I–V* characteristics, as follows:

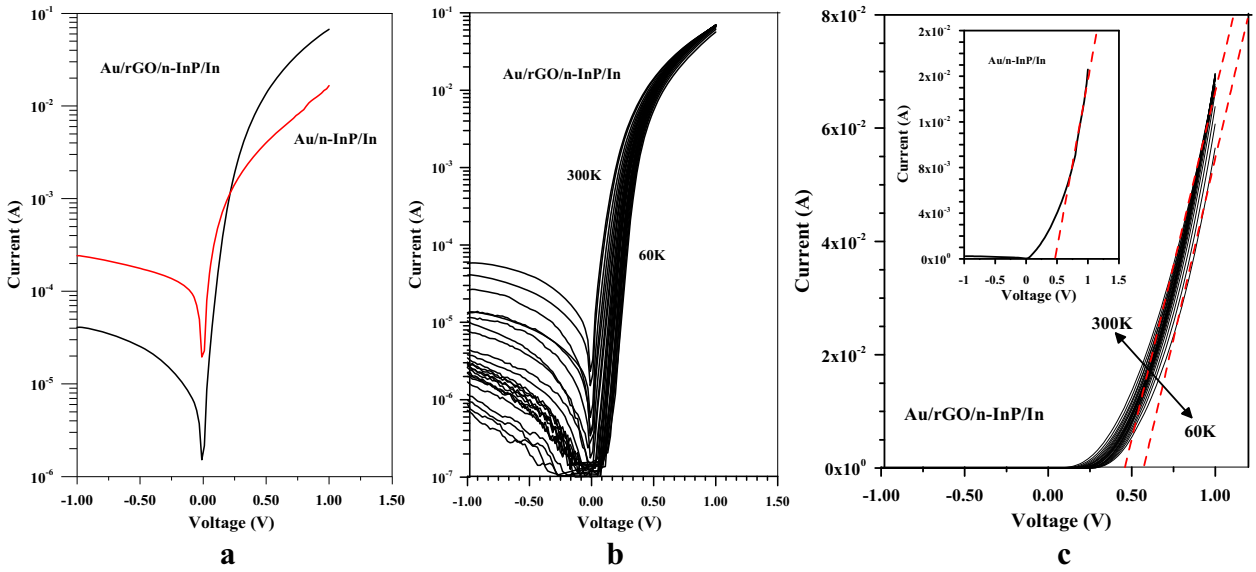



**Fig. 6** Current–voltage characteristics of (**a**) Au/rGO/n-InP/In and Au/n-InP/In Schottky diodes at room temperature, (**b**) Au/rGO/n-InP/In Schottky diode at 60–300 K, and (**c**) Au/rGO/n-InP/In and Au/n-InP/In Schottky diodes at 60–300 K in linear scale

$$I_0 = AA * \ T^2 \ \exp\left(-\frac{q\Phi_b}{kT}\right). \tag{2}$$

In Eqs. 1 and 2, $q$, $n$, $k$, and $T$ are the electron charge, ideality factor, Boltzman's constant, and device temperature, respectively. $A$ is the rectifier contact area of diode, $T$ is the absolute temperature, $A^*$ is the effective Richardson constant of 9.8 $Acm^{-2}$ $K^{-2}$ for n-type InP [16], $\Phi_b$ is the effective barrier height at zero bias between the metal and the semiconductor, and $n$ and $\Phi_b$ can be written as using Eqs. 1 and 2

$$n = \frac{q}{kT}\left(\frac{dV}{d\ln I}\right), \tag{3}$$

$$\Phi_b = \frac{kT}{q}\ln\left(\frac{A^*AT^2}{I_0}\right). \tag{4}$$

$n$ and $\Phi_b$ values for all temperature have been calculated from the linear forward bias ln$I$-$V$ characteristics using Eqs. 3 and 4. The $\Phi_b$ and $n$ values (Fig. 6a) are found to be 0.44 eV and 1.82 for the Au/n-InP reference diode, 0.71 eV and 1.02 for the Au/rGO/n-InP Schottky structures at room temperature. The $\Phi_b$ value of Au/rGO/n-InP Schottky device is almost two times higher when compared to the reference Au/n-InP diode. This may occurred related to the presence of negative fixed charges in the InP and reduced graphene oxide interface close to the InP surface, and also the presence of indium vacancies formed near the InP surface when the interface is being formed [31]. The presence of this negative charge causes an increase in the positive space charge within the depletion region, resulting in the increasing height of the barrier and causing greater band bending. The Au-InP contact barrier may be affected by the change in the surface conditions, which can result in an increase in the barrier height [32]. And ideality factor values are greater than unity for both the Au/n-InP reference diode and the Au/rGO/n-InP Schottky devices. This can be attributed to interface dipoles caused by an interlayer, a specific interface structure, or the presence of the defects at the interface during fabrication process. Moreover, the interface states distributions, the recombination–generation mechanisms, the image force effect, and the tunneling effect may cause an unideal ideality factor [16]. An another reason for unideality of $n$ may be attributed to the barrier height inhomogeneity of the Au/rGO/n-InP contact [16].

According to temperature-dependent $I$-$V$ characteristics (Fig. 6b), n values decreased from 6.77 at 60 K to 1.02 at 300 K with the increasing temperature, $\Phi_b$ values increased from 0.26 at 60 K to 0.71 eV at 300 K. All ideality factor values are higher than ideality ($n > 1$). So, for the Au/rGO/n-InP Schottky diode, there are deviations from the thermionic emission (TE) theory. This abnormality can be attributed to interface states and the barrier inhomogeneity at the interface. In addition, the saturation current increased with the increasing temperature

values for the Au/rGO/n-InP device. Thus, the Au/rGO/n-In device can be used for temperature-dependent applications in technology. As Tung mentioned [20], if barrier height is inhomogeneous, the charge carriers do not have enough energy to pass over the high barrier height at low temperatures. However, current transport is provided by the lower parts of the existing barrier height. In the barrier height inhomogeneity model, the current transport mechanism is considered to be thermionic emission over an inhomogeneous barrier, and this results in increased barrier height and reduced ideality factors with the increasing temperature.

In Fig. 6c, at room temperature, the devices show outstanding performances with a low turn-on voltage (*Vturn-on*) of 0.48 V, and 0.42 V for reference and Au/rGO/n-InP diodes, respectively. The observed low turn-on voltage for Au/rGO/n-InP in comparison to reference Au/n-InP diode (from *I-V* characteristics) may arise as a consequence of lower potential for doping (better dopability), higher concentration of carrier generation mechanisms, and the presence of rGO film and Au/rGO/n-InP diode shows better device performance [33]. As shown in Fig. 6c, as a result of the rGO film, the turn-on voltage of the SBD is improved and the reverse leakage current is reduced.

The series resistance ($R_s$) is one of the important parameters for the evaluation of the performance and the device quality of the Schottky diodes. Series resistance effect becomes predominant at higher bias voltages and causes a decrease in diode current. $R_s$ values of the diodes were calculated by Cheung functions method [34]. The $R_s$ values of Au/n-InP and Au/rGO/n-InP were found to be 8.97 and 7.67 Ω from experimental forward bias *I-V* characteristics at room temperature (300 K). The effects of the series resistance and interface states and the voltage drop across the interfacial rGO layer may cause the different values of ideality factor of the reference Au/n-InP and Au/rGO/n-InP [34]. Also, the series resistance values decreased from 9.28 Ω at 60 K to 7.67 Ω at 300 K with the increasing temperature for the Au/rGO/n-InP device. While the temperature is increasing, the experimental $R_s$ values decreased and the barrier height values are substantially increased as a function of temperature. Furthermore, the higher series resistance $R_s$ value may cause a higher n values.

The turn-on voltage in Fig. 6c gradually decreased from 0.57 V to 0.48 V with the temperature increasing from 60 to 300 K for Au/rGO/n-InP SBD. In addition, the decrease in turn-on voltage and series resistance with increasing temperature due to the effects of the thermal shrinkage of the energy band gap increase the generation of the high energy carriers through interface [35, 36]. The generation of charge carrier through the interface leads to the decrease in depletion layer near the interface. Furthermore, the probability of the thermionic field emission (TFE) cause large leakage current. At higher temperatures, some carriers thermally flow across the Schottky barrier, while some carriers experience a tunneling through the barrier. Both mechanisms may contribute the current transport in the Au/rGO/n-InP device at higher temperatures. Therefore, the temperature-dependent measurements of *I-V* characteristics of the Au/rGO/n-InP device would reveal the carrier transport mechanisms [36].

Considering the model suggested theoretically by Tung, it is suggested that there is a linear relationship between the experimental zero bias SBHs and the ideality factors [37]. Figure 7 shows the experimental BH versus the ideality factor plot at 60–300 K temperature ranges. Here, there are two linear regions

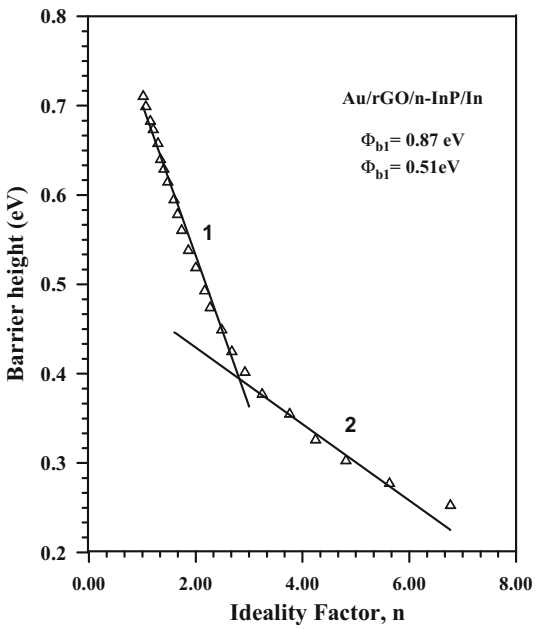



**Fig. 7** The experimental barrier height versus ideality factor values of Au/rGO/n-InP Schottky diode. The region 1 indicates the current controlled by thermionic emission and region 2 indicates current controlled by thermionic field emission

exist between the $\Phi_b$ and $n$ values of the Au/rGO/n-InP Schottky diode structure, which could be attributed to the lateral inhomogeneities of the SBHs. From extrapolation of the experimental $\Phi_b$ and $n$ curve, the homogeneous barrier height values were calculated as $\Phi_{b1}$ = 0.87 eV for the first region (120–300 K) and $\Phi_{b2}$ = 0.51 eV for the second region (60–120 K). That is, under forward bias, the current transport for $T \geq 120$ K is controlled by thermionic emission mechanism, and for $T \leq 120$ K, by the thermionic field emission (TFE) mechanism [22, 38]. Thus, the dominant current transport is not only thermionic emission for Au/rGO/n-InP Schottky diode; instead, there are also two Gaussian distributions (GDs) of the barrier heights in the certain contact area.

Figure 8 shows the traditional Richardson plots of Au/rGO/n-InP Schottky barrier diode. According to Eq. 2, the plot of ln $I_0/T^2$ versus $1/kT$ or $1/nkT$ graphs of Richardson plots must be linear but as shown in Fig. 8, the ln $I_0/T^2$-$1/kT$ is linear up to approximately 180 K and it deviates from linearity with a bowing at low temperatures below 180 K. The slope of this linear region gives the mean barrier height value of 0.97 eV (Eq. 2). Also, the experimental Richardson constant value of $A^*$ is obtained as 11.68 Acm$^{-2}$ K$^{-2}$ from the intercept of this linear fit and for n-InP this experimental $A^*$ value is slightly higher than its theoretical $A^*$ value of 9.8 Acm$^{-2}$ K$^{-2}$ [16]. The spatial inhomogeneous barrier heights and the potential fluctuations at the interface of low and high barrier areas could be the reason for this deviation in the Richardson graph [20, 21]. In these circumstances, the current flows through the lower barriers in the potential distribution. In an ideal MS junction, the barrier height may prefer to follow the variation of band gap with temperature. Although, in ideal conditions, the $n$ value is equal to 1 for a SBD. But, $n$ often has a greater value than the unity, and the SBH is usually a function of temperature. The high values of the ideality factor are attributed to various causes, such as the existence of the interfacial layer, the series resistance effect, and the barrier anomalies [20]. Moreover, the low-temperature $I$-$V$ characteristics of Schottky devices are significantly affected by potential fluctuations. In quantum mechanics, carriers can tunnel through a barrier when exposed to high electric fields. When there is a thermally active tunneling process, the carrier transport mechanism is now referred to as thermionic field emission (TFE) [39]. The Richardson graphs tend to be linear at high temperatures but move away from linearity at low temperatures. The nonlinearity in the Richardson plot was a demonstration of recombination in the depletion region of the Au/rGO/n-InP device. It also makes sense for a device when recombination takes place at low temperatures that this nonlinear state is more observable at low temperatures. With the Richardson graph, the barrier origin is assumed to be a temperature-independent barrier height. These may be due to the inhomogeneous barrier height, often accompanied by ideality factor higher than unity. The temperature-dependent barrier and the ideality factor are also the reason of the nonlinear Richardson graphs [39, 40]. The deviation from the theoretical value of the Richardson constants obtained by the Richardson graph can be explained by high ideality factors and the barrier height inhomogeneity [39].

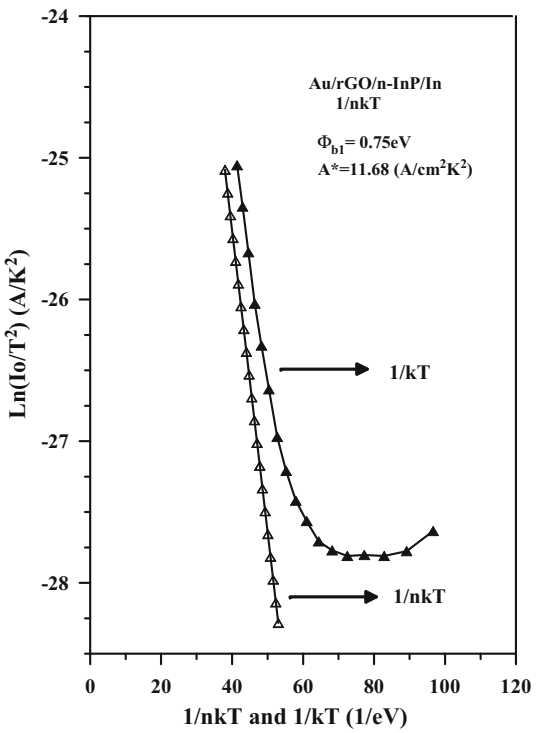



**Fig. 8** The Richardson plots (ln $I_0/T^2$ versus $1/kT$ or $1/nkT$) of Au/rGO/n-InP Schottky diode

Figure 7 shows the existence of the Gaussian distributions of the barrier height for Au/rGO/n-InP SBD. However, the above observations are consistent with the recent model of the lateral distribution of the barrier height [19]. In this model, the decrease in barrier height at low temperatures can be well explained by the thermionic field emission (TFE) if the BH values of the Schottky contact have a good GD

with an average $\overline{\Phi}_{bo}$ value and standard deviation of $\sigma_s$ [7]. Here, $\sigma_s$ indicates the measure of the barrier homogeneity. The experimental $\Phi_{ap}$ and $n_{ap}$ versus ½ $kT$ plots are given in Fig. 9, which indicates two linear regions of approximately 60–120 K and 120–300 K regarding to the TFE over a GD of the barrier height. In such a situation, the $\Phi_{ap}$ is expressed as follows [19]:

$$\Phi_{ap} = \overline{\Phi}_{bo} - \frac{q\sigma_{so}^2}{2kT}, \tag{5}$$

where $\Phi_{ap}$ is the experimentally measured apparent barrier height. Here, $\sigma_s$ can be neglected because its temperature dependency is usually very low [41]. The $n_{ap}$ is given by

$$\left(\frac{1}{n_{ap}} - 1\right) = -\rho_2 + \frac{q\rho_3}{2kT}, \tag{6}$$

where $n_{ap}$ is the experimentally measured apparent ideality factor and $\rho_2$ and $\rho_3$ represent the voltage deformation of the distribution of BH in the nonhomogeneous barrier. The experimental $n_{ap}$-$1/2kT$ plots should be linear (Eq. 6). The values of $\rho_2$ were calculated as 0.54 eV between 120 and 300 K and 0.33 eV between 60 and 120 K temperatures. The linear behavior of the plot shows that the ideality factor expresses the voltage deformation of the Gaussian distribution of the Schottky barrier height [7]. Similarly, the linear $\Phi_{ap}$-$1/2kT$ plot gives the mean

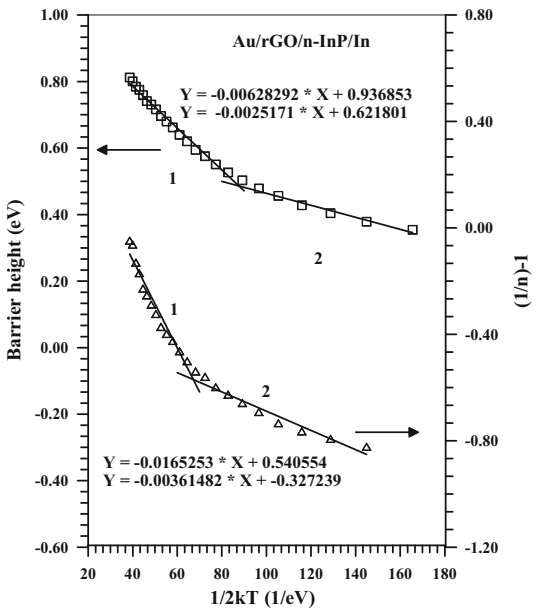



**Fig. 9** The experimental $\Phi_{ap}$ and $n_{ap}$ versus $1/2kT$ plots of Au/rGO/n-InP Schottky diode

barrier height value of $\overline{\Phi}_{bo}$ and $\sigma_s$ from the intercept and slope, respectively. The values of $\overline{\Phi}_{bo}$ and $\sigma_s$ of Au/rGO/n-InP SBD are obtained as 0.93 eV and 0.0063 eV between 120 and 300 K and 0.62 eV and 0.0025 eV between 60 and 120 K temperatures. In addition, standard deviation is a measure of barrier homogeneity, that is, the lower the standard deviation, the closer the homogeneous barrier height is and the better the diode [42]. If $\sigma_s$ values are smaller than $\overline{\Phi}_{bo}$, it indicates an inhomogeneous situation at the interface. These inhomogeneous distribution and potential fluctuations affect low current–voltages. This effect is particularly responsible for the nonlinear behavior on Richardson curves. The above observations indicate the barrier height in the contact area can be modeled with double Gaussian distributions, which represents the high and low barrier of the full distribution in 60–120 K and 120–300 K ranges. The existence of a double Gaussian in Schottky diodes can be attributed to the nature of the inhomogeneities themselves. This may involve variation in the interface composition/phase, interface quality, electrical charges, and nonstoichiometry. They are sufficiently effective to influence the *I-V* characteristics of the Schottky diodes especially at low temperatures. Thus, the *I-V* measurements at low temperatures are capable of revealing the nature of barrier inhomogeneities present in the contact area [37].

There are many models in the literature to explain the charge transmission for different materials, such as Schottky, Poole Frenkel, and space-charge-limited current (SCLC) [43]. Thus, many researchers have conducted their studies on the SCLC mechanism to understand the charge transport through the charging and discharging of the injected carriers from the trap centers [44]. Therefore, the *I-V* characteristics of the reference and Au/rGO /n-InP device were drawn on the log scale shown in Fig. 10 to evaluate existing conduction mechanisms that can control the current transport characteristics of the Schottky diode. In general, the forward bias *log I-log V* plot consists of three different linear regions, showing three distinct conduction mechanisms. When there are deep traps at the interface, the charge transport method and the slope of the *I-V* characteristics get modified. The linear region I is the region of low voltages and indicates that the structure shows an ohmic character. In other words, the current changes

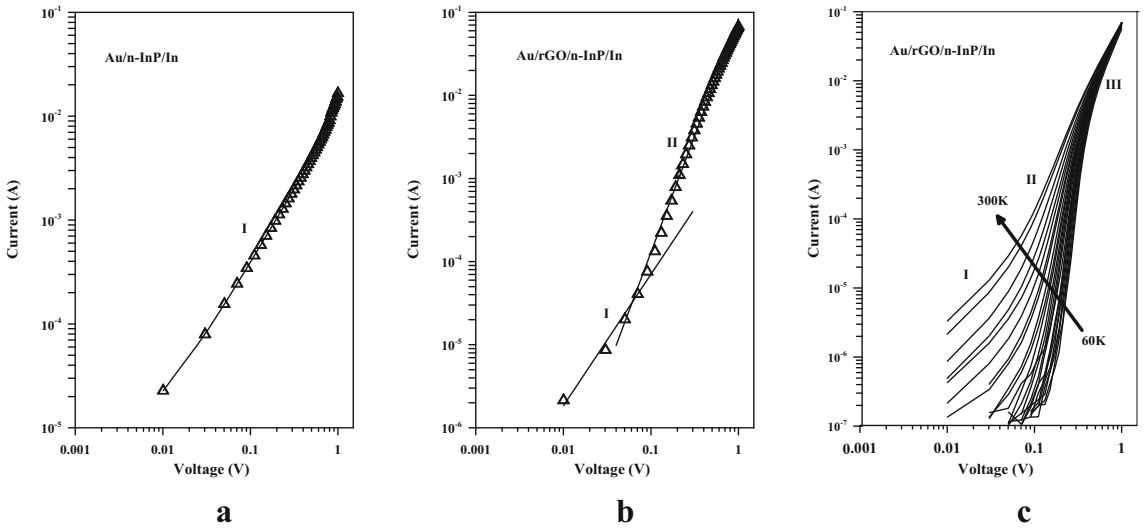



**Fig. 10** *log I-logV* graph of (**a**) Au/n-InP reference diode, (**b**) Au/rGO/n-InP Schottky diode at room temperature, and (**c**) Au/rGO/n-InP Schottky diode at 300–60 K

directly by the applied voltage and the free charge carriers are more than the carriers injected into the material due to the low bias voltage. From Fig. 10a, this double logarithmic graph indicates that the conduction mechanism in the reference Au/n-InP device is almost ohmic conduction. The linear region II is the region of higher voltages and in this case, there is a nonnegligible concentration of charge carriers injected to the semiconductor material with applied voltage due to the presence of the traps in the thin film [45]. Therefore, a space-charge-limited current (SCLC) mechanism occurs. While the current in the ohmic region changes with the $V$ value, the current in this SCLC region changes with the $V^2$ value. At the same time, the lower traps are effective in this region and the injected free carriers cause the SCLC conduction mechanism. We can say that the SCLC mechanism becomes dominant when the density of injected or triggered free charge carriers is much greater than that of thermally formed free carriers at the equilibrium charge concentration [46]. Also, the SCLC model is widely used to describe the behavior of organic Schottky diodes [46]. From Fig. 9b, we can conclude that the carrier transport mechanism is controlled by SCLC model at room temperature. In the region III of even higher voltages, the effective trap conditions contribute to current as well as injected carriers. At high voltage values, the traps begin to fill with the increase in SCLC current and the Schottky device approaches the "trap-filled" limit. In the literature the trap-filled SCLC is also known as trap-charge-limited current (TLCL). As a consequence, the current conduction occurs again by a SCLC mechanism in this region [47]. As shown in Fig. 10c, the slope of the region III increased with the decreasing temperature in the Au/rGO/n-InP device with rGO interlayer. It is undoubted that the interface plays an important role in the serial resistance and electronic properties of the device, and it has affected the trapped space-charge-limited current mechanism depending on the sample temperature. When the sample temperature increases, the recombination in the rGO layer can be triggered thermally, and as a result, it has a high resistance state. Hence, in the trapped SCLC region, the series resistance increased with the increasing temperature.

## 4 Conclusion

In this study, in order to fabricate the Au/rGO/n-InP SBD, firstly, the reduced graphene oxide (rGO) was synthesized from graphene oxide (GO) by a chemical reduction method and then the simple and cheap spray pyrolysis technique was used to obtain reduced graphene oxide film. The XRD, SEM, and UV–Vis spectroscopies were used for characterization of structural, morphological, and optical properties of reduced graphene oxide film. From *I-V* characteristics of the Au/rGO/n-InP SBD in the temperature ranges from 60 to 300 K with 10 K steps, the device parameters of barrier height and ideality

factor are found to be strong functions of temperature due to the barrier inhomogeneities at metal–semiconductor interface. The presence of reduced graphene oxide film results in lower turn-on voltage and reverse leakage current for Au/rGO/n-InP Schottky diodes. The Au/rGO/n-InP device has been shown to good rectifying properties, low turn-on voltage, and low leakage current, resulting in better device performance when compared to the Au/n-InP reference diode. The barrier height potential at the metal–semiconductor interface is not homogeneous, and it is explained by the barrier inhomogeneity model. The temperature dependency of the electrical characteristics of the Au/rGO/n-InP SBD was explained by the thermionic field emission (TFE) theory with Gaussian distribution of the barrier height values. In this model, the Schottky barrier height has a Gaussian distribution of the barrier height values over the Schottky contact area with a mean barrier height of $\overline{\Phi}_{bo}$ = 0.93 eV at 120–300 K temperatures and $\overline{\Phi}_{bo}$ = 0.62 eV at 60–120 K temperatures. Furthermore, the forward *log I-log V* plots of the device showed three regions. At lower bias values, the ohmic conduction mechanism attributed to the tunneling of charge carriers at the interfaces in region I. At higher bias values, a SCLC mechanism of the space-charge-limited current is the dominant current transport mechanism in regions II and III. In conclusion, the existing current mechanism is predominantly controlled by SCLC mechanism for Au/rGO/n-InP SBD and the reduced graphene oxide interface plays an important role in the conduction mechanism and electronic properties of the Au/rGO/n-InP device.

## References


1. H. Zhao, Q. Guo, F. Xia, H. Wang, Nanophotonics **4**, 128–142 (2015)
2. H. Darrudi, M. Adelifard, Iran. J. Mater. Sci. Eng. **16**, 22–28 (2019)
3. K. Kanishka, H. De Silva, H.-H. Huang, S. Suzuki, M. Yoshimura, Jpn. J. Appl. Phys. **58**, SIIB07 (2019)
4. M.S. Poorali, M.M. Bagheri-Mohagheghi, J. Mater. Sci. Mater. Electron. **27**, 260–271 (2015)
5. A. Turut, A. Karabulut, K. Ejderha, N. Bıyıklı, Mater. Sci. Semicond. Process **39**, 400–407 (2015)
6. M. Gülnahar, Metall. Mater. Trans. A **46**, 3960–3971 (2015)
7. F.E. Cimilli, M. Sağlam, H. Efeoğlu, A. Türüt, Physica B **404**, 1558–1562 (2009)
8. A. Kocyigit, I. Orak, Z. Çaldıran, A. Turut, J. Mater. Sci. Mater. Electron. **28**, 17177–17184 (2017)
9. I. Jyothi, V. Janardhanam, J.-H. Kim, H.-J. Yun, J.-C. Jeong, H. Hong, S.-N. Lee, C.-J. Choi, J. Alloys Compd. **688**, 875–881 (2016)
10. Z. Khurelbaatar, Y.-H. Kil, H.-J. Yun, K.-H. Shim, J.T. Nam, K.-S. Kim, S.-K. Lee, C.-J. Choi, J. Alloys Compd. **614**, 323–329 (2014)
11. M. Zhu, X. Li, Y. Guo, X. Li, P. Sun, X. Zang, K. Wang, M. Zhong, D. Wu, H. Zhu, Nanoscale **6**, 4909 (2014)
12. G.G. Batır, M. Arık, Z. Caldıran, A. Turut, S. Aydogan, J. Electron. Mater. **47**, 329–336 (2017)
13. S.N.C. Azmi, S.F.A. Rahman, A. Nawabjan, A.M. Hashim, Microelectron. Eng. **196**, 32–37 (2018)
14. B. Pandit, J. Cho, Thin Solid Films **660**, 824–827 (2018)
15. J. Wilson, J. Zhang, A. Song, A.C.S. Appl, Electron. Mater. **1**, 1570–1580 (2019)
16. F.E.C. Çatır, Semicond. Sci. Technol. **35**, 035023 (2020)
17. F. E. Cimilli, H. Efeoğlu, M. Sağlam, A. Türüt, J. Mater. Sci. Mater. Electron. **20**, 105–112 (2008)
18. B. Güzeldir, M. Sağlam, A. Ateş, J. Alloys Compd. **506**, 388–394 (2010)
19. J. H. Werner, H. H. Güttler, J. Appl. Phys. **69**, 1522–1533 (1991)
20. R. T. Tung, Appl. Phys. Lett. **58**, 2821–2823 (1992)
21. J. Sullivan, R. Tung, M. Pinto, W. Graham, J. Appl. Phys. **70**, 7403–7424 (1991)
22. E. H. Rhoderick, R. H. Williams, Metal-semiconductor Contacts. Clarendon Press, Oxford University Press (1988)
23. E. Özavcı, S. Demirezen, U. Aydemir, Ş. Altındal, Sens. Actuator A Phys. **194**, 259–268 (2013)
24. O. Çiçek, Ş.Altındal, Y. Azizian-Kalandaragh, IEEE Sens. J. 1–1 (2020)
25. Y. P. Song, R. L. Van Meirhaeghe, W. H. Laflère, F. Cardon, Solid-State Electron. **29**, 633–638 (1986)
26. M. Das, J. Datta, A. Dey, S. Halder, S. Sil, P. P. Ray, Mater. Lett. **204**, 184–187 (2017)
27. S. N. Alam, N. Sharma, L. Kumar, Graphene **06**, 1-18 (2017)
28. Q. D. A. Cardoso, J. C. S. Casini, L. P. Barbosa, M. M. Serna, E. Galego, L. F. Sobrinho, S. K. Sakata, R. N. de Faria Jr, Mater. Sci. Forum **958**, 117–122 (2019)
29. L.A. Falkovsky, J. Phys. Conf. Ser. **129**, 012004 (2008)
30. E. Marıl, A. Kaya, H. Çetinkaya, S. Koçyiğit, Ş. Altındal, Mater. Sci. Semicond. Process. **39**, 332–338 (2015)
31. V. R. Reddy, M. S. P. Reddy, B. P. Lakshmi, A. A. Kumar, J. Alloys Compd. **509**, 8001–8007 (2011)
32. A. Cowley, S. Sze, J. Appl. Phys. **36**, 3212–3220 (1965)

33. L.-M. Huang, T.-C. Wen, A. Gopalan, F. Ren, Mater. Sci. Eng. B **104**, 88–95 (2003)
34. S. K. Cheung, N. W. Cheung, Appl. Phys. Lett. **49**, 85–87 (1986)
35. T.-H. Yang, H. Fu, H. Chen, X. Huang, J. Montes, I. Baranowski, K. Fu, Y. Zhao, J. Semicond. **40**, 012801 (2019)
36. V. N. Reddy, M. S. P. Reddy, K. Gunasekhar, J.-H. Lee, Appl. Phys. A **124** 291 (2018)
37. S. K. Chand, J. Kumar, Appl. Phys. A **63**, 171–178 (1996)
38. S. M. Sze, K. K. Ng, Physics of Semiconductor Devices. John Wiley & Sons, Hoboken (2006)
39. Ö. Metin, Ş. Aydoğan, K. Meral, J. Alloys Compd. **585**, 681–688 (2014)
40. D. K. Schroder, Semiconductor Material and Device Characterization. John Wiley & Sons, Hoboken (2015)
41. C. Coskun, M. Biber, H. Efeoglu, Appl. Surf. Sci. **211**, 360–366 (2003)
42. M. A. Mayimele, J. P. J. van Rensburg, F. D. Auret, M. Diale, Physica B **480**, 58–62 (2016)
43. K. C. Kao, W. Hwang, Electrical Transport in Solids: With Particular Reference to Organic Semiconductors. Pergamon Press (1981)
44. İ. Taşçıoğlu, W. Farooq, R. Turan, Ş. Altındal, F. Yakuphanoglu, J. Alloys Compd. **590**, 157–161 (2014)
45. S. Guessasma, M. Chahdi, Mater. Sci. Semicond. Process. **7**, 411–417 (2004)
46. S. Zhu, R. Van Meirhaeghe, S. Forment, G. Ru, B. Li, Solid-State Electron. **48**, 29–35 (2004)
47. A. Bengi, U. Aydemir, Ş. Altındal, Y. Özen, S. Özçelik, J. Alloys Compd. **505**, 628–633 (2010)

**Publisher's Note** Springer Nature remains neutral with regard to jurisdictional claims in published maps and institutional affiliations.